

# Graphene–amorphous carbon with interwoven networks for enhanced strength

Received: 11 January 2025

Accepted: 24 October 2025

Published online: 26 November 2025

Check for updates

Wanxiaonan Chen <sup>1,2,3,4</sup>, Jie Sheng <sup>1,2,3</sup> ✉, Daming Chen<sup>2</sup>, Boqian Sun<sup>2</sup>, Hao Ding<sup>1</sup>, Linsen Zhang<sup>1</sup>, Bin Liu<sup>1</sup>, Qingtan Ren <sup>1</sup>, Deyu Zhang<sup>1</sup>, Yuhao Fang<sup>2</sup>, Xianchao Lu<sup>1</sup>, Yuying Wu<sup>1</sup>, Yang Lan<sup>1</sup>, Yongchun Zou<sup>5</sup>, Peng Zhang<sup>6</sup>, Xiaomeng Yang<sup>7</sup>, Pengcheng Zhang<sup>6</sup>, Zhiqi Wang <sup>1</sup>, Qianru Lin<sup>1,3</sup>, Mingyi Tan<sup>2,4</sup>, Wenzheng Zhang<sup>2,4</sup>, Yuan Cheng<sup>2,4</sup>, Weili Li<sup>1</sup>, Lidong Wang <sup>1</sup> ✉, Shun Dong<sup>2,4</sup>, Shanyi Du<sup>2</sup>, Jiecai Han<sup>2</sup>, Weidong Fei <sup>1</sup> ✉ & Xinghong Zhang<sup>2,4</sup> ✉

High-strength, high-conductivity graphite-based carbon materials (GCMs) are widely explored for diverse applications. Designing and regulating the graphitic phase microstructure is essential for simultaneously enhancing mechanical and electrical properties, particularly mechanical strength. Here, we propose a two-step strategy to synthesize graphene-amorphous carbon (GAC) with interwoven graphene networks. By leveraging the different graphitization tendencies between polyacrylamide and glucose, we obtained GAC with a microscale structure in which few-layers graphene and amorphous carbon are uniformly interwoven. Therefore, the GAC exhibits exceptional compressive and flexural strengths of 303 MPa and 203 MPa, respectively, greatly exceeding previously reported performance benchmarks. Microscopic studies reveal that crack propagation is significantly impeded by the network of cross-cutting few-layer graphene, resulting in continuous crack deflections, which account for the outstanding mechanical performance of the GAC. This microstructure design strategy provides the rationale for developing ultrahigh-strength GCMs.

The diverse bonding configurations of carbon atoms give rise to a wide range of allotropes, with complex bonding arrangements leading to diverse structural characteristics and physical properties<sup>1–6</sup>. Among them, graphite-based carbon material (GCM) has attracted considerable attention for its broad applicability, owing to its excellent conductivity derived from the  $sp^2$  bonding structure<sup>3,5</sup>. Nevertheless, optimizing their structural design and enhancing their mechanical performance for advanced applications continues to be a major challenge<sup>1,3,5</sup>.

Traditionally, the preparation of high-density GCM requires coke and binders as starting materials, followed by a complicated and lengthy carbonization and graphitization<sup>7–10</sup>. Current methods for improving traditional GCM microstructures primarily involve the following approaches. First, chemical techniques are employed to purify the starting materials from petroleum coke, preventing the formation of large graphite grains<sup>11</sup>, which effectively enhances the mechanical properties of GCM. Second, both doping strategies and reinforcement addition have made significant progress in optimizing GCM

<sup>1</sup>School of Materials Science and Engineering, Harbin Institute of Technology, Harbin, China. <sup>2</sup>National Key Laboratory of Science and Technology on Advanced Composites in Special Environments, Harbin Institute of Technology, Harbin, China. <sup>3</sup>Laboratory for Space Environment and Physical Sciences, Harbin Institute of Technology, Harbin, China. <sup>4</sup>Suzhou Laboratory, Suzhou, China. <sup>5</sup>Center of Analysis and Measurement, Harbin Institute of Technology, Harbin, China. <sup>6</sup>State Key Laboratory for Mechanical Behavior of Materials, Xi'an Jiaotong University, Xi'an, China. <sup>7</sup>Department of Materials Science and Engineering, Southern University of Science and Technology, Shenzhen, China. ✉ e-mail: [shengjie@hit.edu.cn](mailto:shengjie@hit.edu.cn); [wld@hit.edu.cn](mailto:wld@hit.edu.cn); [wdfei@hit.edu.cn](mailto:wdfei@hit.edu.cn); [zhanghx@hit.edu.cn](mailto:zhanghx@hit.edu.cn)

performance: the former improves thermomechanical properties by promoting graphitization—for instance, Li et al.<sup>12</sup> introduced silicon atoms to bridge graphene layers through the formation of Si-C bonds and Y-type carbon structures, which guide the alignment of graphite layers and enhance structural order; Liu et al.<sup>13</sup> found that co-doping with Si and Ti can act as a catalyst to accelerate graphitization, thereby enhancing crystallinity, reducing porosity, and improving thermal conductivity. The latter has achieved remarkable results in the development of graphite-based composites<sup>5,14–16</sup>: for example, the addition of 1% sulfonated graphene into petroleum coke powder results in GCM with flexural and compressive strengths of 57 MPa and 121 MPa, respectively<sup>14</sup>. High-density bulk GCM, formed by converting diamond filler into onion-like carbon during high-temperature sintering<sup>3,5,17</sup>, achieves a flexural strength of 69.6 MPa. This strength is attributed to the formation of  $sp^3$  hybrid bonds between graphite layers, which prevent interlayer cleavage<sup>15,18</sup>. Additionally, GCM prepared with cold isostatic pressing technology demonstrates more consistent mechanical properties<sup>19–21</sup>. The findings of Gracia provide a critical theoretical foundation for understanding the transition from  $sp^2$  to  $sp^3$  hybridization under the condition of high pressure<sup>3,17,22–24</sup>, while also enabling the design of microstructures in carbon materials. GCM sintered under 2.4 GPa of pressure exhibits flexural and compressive strengths of 110.3 MPa and 208.1 MPa, respectively<sup>25</sup>.

Figure 1a illustrates the relationship between the flexural and compressive strength of GCM over recent decades (see Supplementary Table 1 for data sources). Generally, these strengths exhibit a roughly linear correlation. Microstructures obtained through conventional methods typically consist of nanographite crystals uniformly nucleated within amorphous carbon. However, these methods provide limited control over the morphology and structure of the graphite crystals, leading to a bottleneck for further improving flexural performance of GCM. Therefore, it is essential to design and incorporate new microstructures.

Recently, advancements in the synthesis of carbon-based materials, including fibers, aerogels, and composites, have utilized glucose

as a carbon source through gel pyrolysis<sup>18,26–29</sup>. These sugar-derived GCM demonstrates excellent mechanical properties at both the micro- and nano-scales. However, significant shrinkage and stress during carbonization lead to the formation of cracks and pores, complicating the production of bulk materials at the macroscopic scale in a single step. Here, we propose a two-step strategy (Fig. 1b) to synthesize high-strength graphene-amorphous carbon (GAC) using polyacrylamide (PAM) and glucose (GLC) hydrogels as starting materials. PAM, which forms the gel network structure within the composite hydrogel, was found to preferentially undergo graphitization. By exploiting the differing graphitization tendencies of PAM and glucose, we successfully developed a GAC with a random interwoven graphene networks structure, in which few-layer graphene forms a continuous, intersecting network. Notably, PAM, due to its nitrogen content, undergoes graphitization more readily, promoting the formation of  $sp^2$  bonds<sup>4,30–32</sup>. In contrast, glucose is less prone to graphitization and tends to yield an amorphous carbon structure with a mixed  $sp^2/sp^3$  bonding character<sup>26,33,34</sup>. The spatial configuration of these two precursors plays a critical role in determining the distribution of  $sp^2$  and  $sp^3$  bonds within the material, thereby influencing the mechanical and electrical properties of the GAC. Therefore, the obtained carbon achieved a compressive strength of 303 MPa and a flexural strength of 203 MPa, surpassing the linear relationship observed in traditional GCM and greatly exceeding the mechanical properties reported to date (Fig. 1a). This approach presents a new pathway for developing high-strength GCM.

## Results and discussion

In this study, PAM and glucose (GLC) were selected as starting materials. Taking into account the optimized cross-linking effect of PAM, along with the material's densification and formability from previous studies<sup>18,26</sup>, the PAM-to-GLC ratio was set at 30%. This optimized ratio facilitates the formation of a dense and stable structure, suitable for effectively tuning the  $sp^2$  to  $sp^3$  carbon ratio through subsequent pre-treatment and spark plasma sintering (SPS). The bulk carbon material

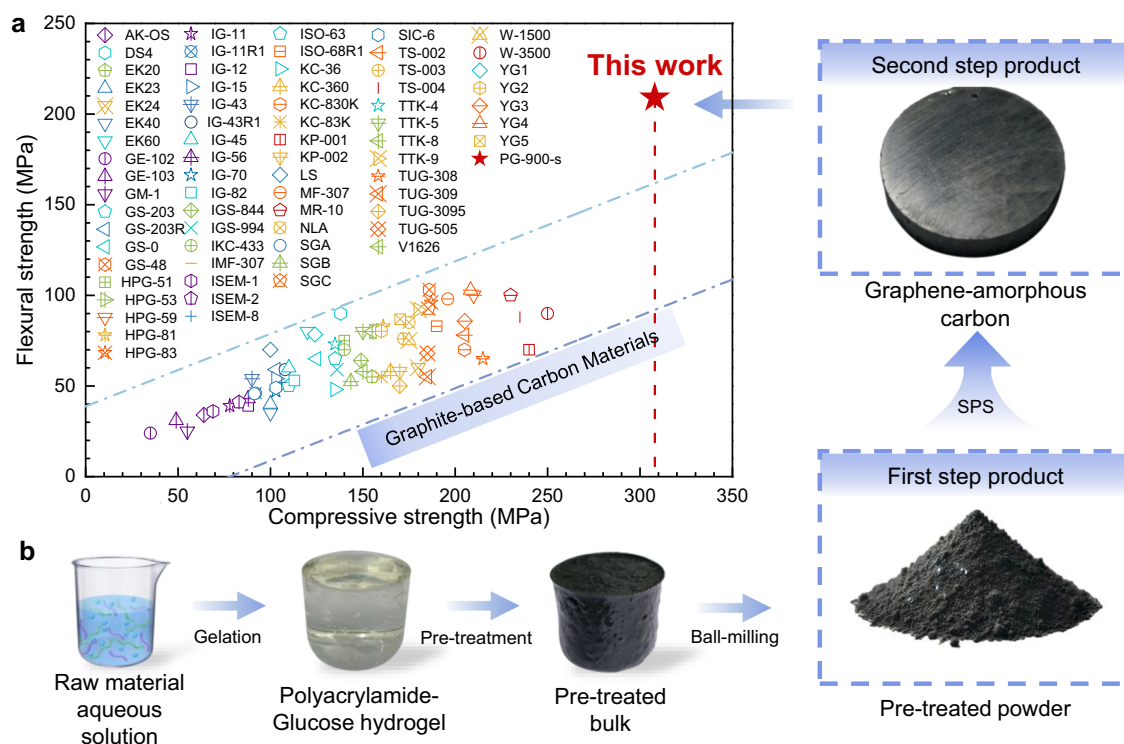


**Fig. 1 | Comparison of the mechanical properties and preparation routes of the GCM in the present study.** **a** Comparison of compressive and flexural strengths (references are listed in Supplementary Table 1). **b** Schematic diagram of the preparation process of GAC in this study. Source data are provided as a Source Data file.

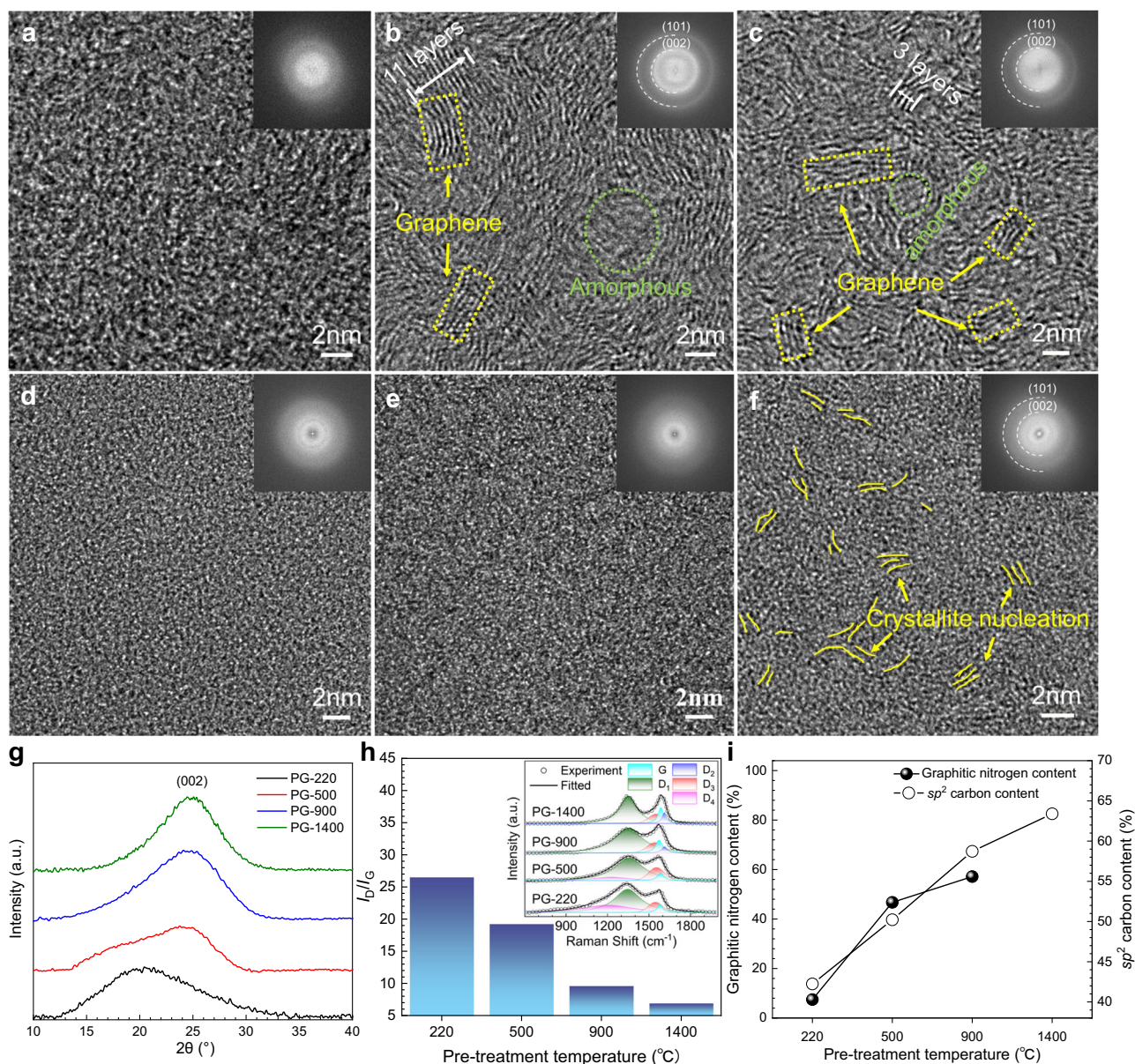


**Fig. 2 | Characterization of pre-treatment powders. a–c** HRTEM images of GLC-1400, PAM-1400, and PG-1400, with insets showing the corresponding SAED patterns. Here, GLC, PAM, and PG denote glucose, polyacrylamide, and polyacrylamide (PAM) and glucose (GLC) hydrogels, respectively, and the numerical values indicate the pre-treatment temperatures of the samples. **d–f** HRTEM images

of PG-220, PG-500, and PG-900, with insets showing the corresponding SAED patterns. **g** XRD patterns analysis of different samples. **h** Comparison of  $I_D/I_G$ ; inset shows fitted Raman peak. **i** Comparison of graphitic nitrogen content and  $sp^2$  carbon content. Each experiment in Figures **a–f** was independently repeated three times with similar results. Source data are provided as a Source Data file.

was prepared using a two-step method (Fig. 1b): firstly, the gelled mixture of PAM and GLC was pretreated, followed by SPS sintering of the pretreated powders. Detailed preparation procedures are provided in the Methods section.

To elucidate the differences in pre-treatment effects on the structures of PAM, GLC, and their mixture (PG), all samples were pretreated at 1400 °C for 1 hour. The respective products, labeled GLC-1400, PAM-1400, and PG-1400, were characterized to highlight the distinct microstructural transformations during pre-treatment. Figure 2a–c show high-resolution transmission electron microscopy (HRTEM) images, along with insets of the selected area electron diffraction (SAED) patterns. The pre-treated GLC product, commonly classified as hard carbon<sup>35</sup>, predominantly comprises amorphous carbon. After pre-treatment at 1400 °C, PAM exhibits a distinct network of thick graphene structures, approximately 11 layers in thickness (Fig. 2b). This suggests that PAM is more susceptible to graphitization

than GLC, a finding further supported by XRD and Raman spectroscopy analyses (Supplementary Figs. 4a and 5). Notably, cryo-SEM images reveal that the PG hydrogel exhibits a highly interconnected 3D open-cell network structure. To further elucidate this morphology, cryo-SEM characterization was performed along three orthogonal directions<sup>36</sup>. As shown in Supplementary Fig. 6, the hydrogel exhibits uniform isotropic porosity from all perspectives. The porosity values measured from the top, left, and front views are 70.12%, 74.21%, and 72.32%, respectively, corroborating its potential as a structurally continuous carbon precursor. This porous network contributes significantly to the continuity observed in pre-treated PAM-derived carbons. As shown in Fig. 2c, the PG-1400 powder forms a structure in which few-layer graphene and amorphous carbon are uniformly interwoven. The few-layer graphene in PG-1400 is significantly thinner (around 3 layers) than that in PAM-1400. The amorphous carbon derived from GLC is embedded in the networked graphene converted

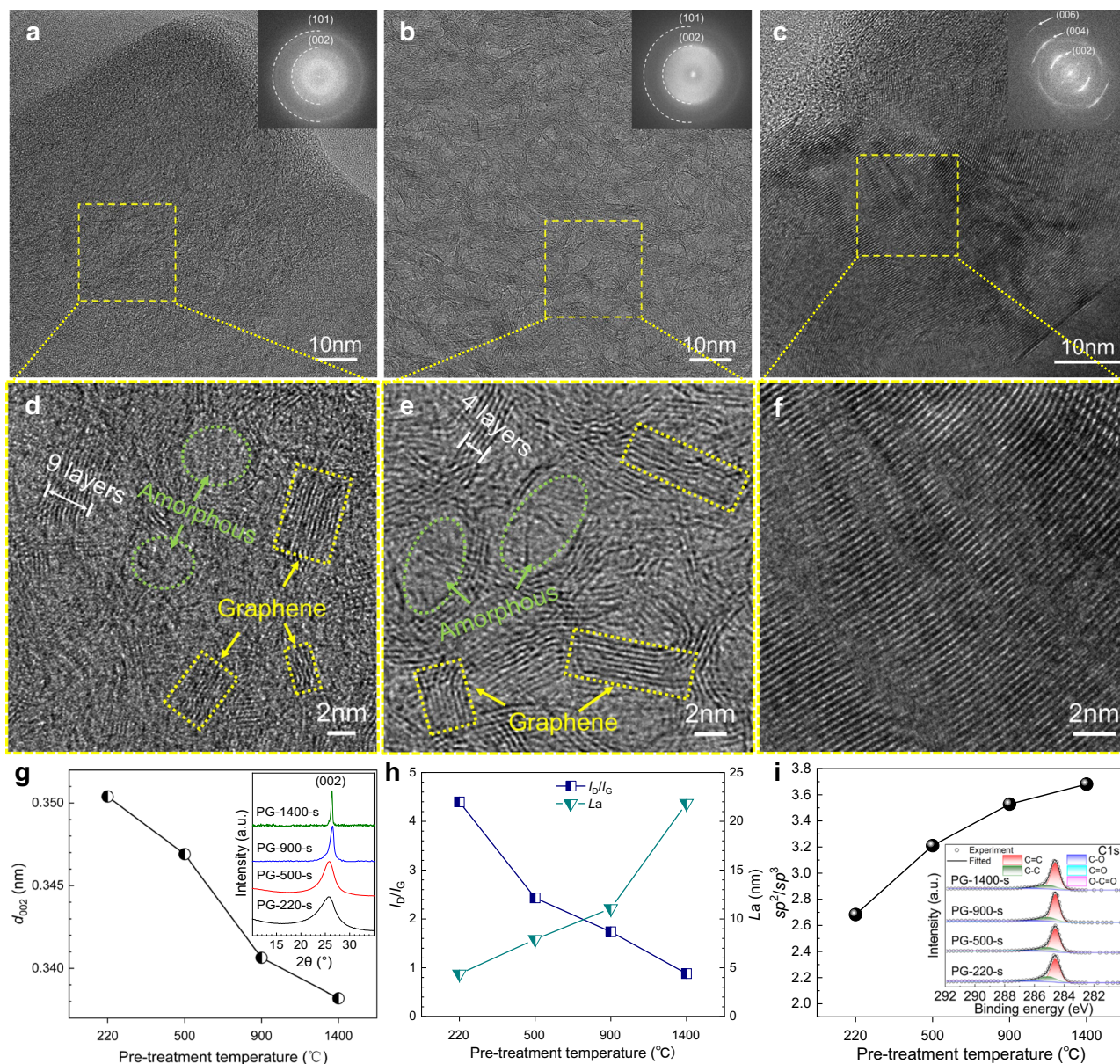


**Fig. 3 | Microstructure and formation mechanism of SPS-sintered samples.** **a–c** HRTEM images of PG-500-s, PG-900-s, and PG-1400-s, with three insets in each image showing the corresponding SAED patterns. **d–f** Magnified views of the yellow boxes in **a–c**, respectively. **g** Comparison of interlayer spacing  $d_{002}$ ; the inset shows

the XRD comparison. **h** Comparison of  $I_D/I_G$  and graphitic crystallite lateral size  $L_a$ . **i** Ratio of  $sp^2$  to  $sp^3$  in XPS spectra; the inset shows XPS peak fitted for C1s. Each experiment in Figures **a–f** was independently repeated three times with similar results. Source data are provided as a Source Data file.

from PAM, preventing further merging and thickening of the PAM-derived few-layer graphene. Therefore, the combination of PAM and GLC facilitates the formation of a continuous few-layer graphene network.

PG gelation was subjected to treatments at 220 °C, 500 °C, and 900 °C to investigate the effects of pre-treatment on the microstructure of the resulting PG powder, referred to as PG-220, PG-500, and PG-900, respectively. As illustrated in Fig. 2d–f, PG gelation gradually transforms into a mixture of nanocrystals and amorphous carbon as the pre-treatment temperature increases, leading to a progressive increase in both the content and size of the nanocrystals (Supplementary Fig. 7a). SAED results further confirm this trend. The XRD patterns in Fig. 2g show that after pre-treatment at 220 °C, the sample consists primarily of amorphous carbon. As the pre-treatment temperature rises, the graphite crystal content gradually rises. Changes in the Raman peak shapes and the  $I_D/I_G$  ratio (Fig. 2h) indicates that

the content of graphite nanocrystals in the composite powder increases, while structural defects decrease as the pre-treatment temperature rises (Supplementary Fig. 7b). XPS results (Fig. 2i) further reveal that pyrrolic and pyridinic nitrogen species progressively convert to graphitic nitrogen, while the proportion of  $sp^2$  hybridized bonds increases with higher pre-treatment temperatures. This suggests that nitrogen facilitates the graphitization process, consistent with the results shown in Supplementary Figs. 4 and 5. Consequently, even at 1400 °C, pre-treated nitrogen-containing polyacrylamide forms few-layer graphene<sup>32</sup>, whereas GLC predominantly converts to amorphous carbon<sup>35</sup>.

PG-220, PG-500, PG-900, and PG-1400 powders were utilized to fabricate the GACs ( $\phi$ 20 mm) through SPS technology (see Methods section). The resulting bulk carbon materials are labeled PG-220-s, PG-500-s, PG-900-s, and PG-1400-s, respectively. To further elucidate the detailed microstructural characteristics of these bulk carbon materials

after SPS treatment under various pre-treatment conditions, polished micrographs were also analyzed (Supplementary Fig. 8). The observed microstructural variations clearly illustrate that pre-treatment temperature critically influences the densification and structural uniformity of the final materials.

The PG-220 powder retains significant amounts of organic functional groups (Supplementary Fig. 9 and 10), and gas byproducts generated during the SPS process create numerous pores, resulting in poor material formability. The HRTEM images of PG-220-s (Supplementary Figs. 11 a, b), PG-500-s, PG-900-s, and PG-1400-s are shown in Fig. 3a–f. PG-220-s primarily consists of amorphous carbon and graphite nanocrystals. Compared to PG-220-s, PG-500-s exhibits larger and more abundant graphite nanocrystals, along with a significant presence of graphene sheets (Fig. 3a, d). In PG-900-s, a substantial amount of few-layer graphene (ranging from 2 to 9 layers) and amorphous carbon collectively form a randomly interwoven network structure<sup>17,32,37,38</sup> (Fig. 3b, e and Supplementary Fig. 11c, d), which markedly differs from the microstructure of conventional GCM. In contrast, PG-1400-s exhibits a highly ordered graphite layer structure, with several dozen layers and uniform interlayer spacing (Fig. 3c, f), closely resembling the structure of traditional GCM.

Figure 3g displays the graphite (002) interlayer spacing, with the inset providing an XRD comparison of the GACs. As the pre-treatment temperature rises, the diffraction peak corresponding to graphite (002) becomes sharper and shifts to a higher angle, indicating enhanced graphitization degree. Supplementary Fig. 12a presents the Raman spectra of the GACs, and Fig. 3h concludes the evolution of the  $I_D/I_G$  ratio and  $L_a$ , while changes in the  $I_{2D}/I_G$  ratio and 2D peak position are detailed in Supplementary Fig. 12b. Higher pre-treatment temperatures yield a lower D peak intensity and higher 2D peak intensity (Supplementary Fig. 12), indicating fewer defects and a greater degree of graphitization.

Considering the significant noise introduced by amorphous carbon, the  $L_a$  value was derived from Raman spectra using a five-peak fitting approach<sup>17,39</sup>. The  $I_D/I_G$  ratio was determined by integrating the fitted D and G bands within the 1000–1800  $\text{cm}^{-1}$  range of the Raman spectrum, and subsequently calculated  $L_a$  based on the empirical equation proposed by Cançado et al.<sup>40</sup>. Notably, the  $L_a \times I_D/I_G$  value obtained under a 532 nm laser wavelength is approximately 19, which primarily depends on the wavelength used during Raman measurements<sup>40</sup>. This result shows great agreement with the pyrolyzed carbon materials that adopt similar peak-fitting strategies<sup>29,41</sup>, supporting the reliability and consistency of our spectral interpretation method. The decrease in the  $I_D/I_G$  ratio and the increase in  $L_a$ , particularly the significant increase to over 20 nm in the PG-1400-s sample, correspond to the formation of thicker graphite layers. The rise in the  $I_{2D}/I_G$  ratio and the minimum 2D peak Raman shift at 900 °C suggest the formation of few-layer graphene. The blueshift of the 2D peak to approximately 2700  $\text{cm}^{-1}$  after treatment at 1400 °C indicates the development of larger graphite layers. The deconvolution of the C1s peak in the XPS data (Supplementary Fig. 13) reveals the evolution of the  $sp^2/sp^3$  hybridization ratio (Fig. 3i), with detailed XPS results shown in the inset of Fig. 3i. Higher pre-treatment temperatures result in a greater  $sp^2$  bond content, aligning with the observed trend of increased graphitization.

The analysis indicates that pre-treatment temperature has a substantial impact on the microstructures of bulk materials prepared by the SPS method. The nanocrystalline graphite formed during pre-treatment serves as nucleation sites for graphene or graphite formation during the SPS process. When pre-treated at 900 °C, PAM predominantly transforms into nanocrystalline graphite, facilitating further development of a few-layer graphene network during SPS. In contrast, pre-treated at 1400 °C converts PAM into thicker and larger graphene sheets, resulting in the formation of large graphite flakes during SPS sintering.

Figure 4a shows the density of the sintered GACs. PG-220-s and PG-1400-s exhibit lower densities, while PG-500-s and PG-900-s achieve higher densities. To further elucidate the origins of the observed density variations, we analyzed the surface morphologies of SPS-sintered samples and performed mercury intrusion porosimetry (Supplementary Figs. 8 and 14). The results clearly show that the relatively low densities of PG-220-s and PG-1400-s stem from their significantly higher porosity, caused by incomplete decomposition of organic species and diminished sintering activity due to over-graphitization, respectively. Highly graphitized carbon powders are challenging to sinter due to limited atomic diffusion and rearrangement. In contrast, amorphous carbon, with its defects and irregular structure, facilitates atomic movement and reorganization at high temperatures, thereby improving self-sintering properties. Figure 4b–d show the properties of GACs prepared at various pre-treatment temperatures. PG-900-s exhibits the best overall performance, with a flexural strength of 203 MPa and a compressive strength of 303 MPa, both significantly higher than those of traditional GCM. PG-900-s also demonstrates an elastic modulus of 20.12 GPa, a hardness of 1.80 GPa (Supplementary Fig. 15), and an electrical conductivity of  $3.84 \times 10^4 \text{ S/m}$ . The elastic modulus and hardness reported in Fig. 4c were obtained from nanoindentation tests using a Berkovich tip at 10 mN load. Each sample was tested at three different locations, and the average values were used. The hardness and modulus were calculated using the Oliver–Pharr method<sup>42</sup>.

The excellent performance of PG-900-s is attributed to its unique graphene-amorphous carbon random interwoven graphene network structure. Notably, the PG-900-s sample demonstrates performance comparable to or exceeding that of conventional pyrolytic carbon (PyC)<sup>43–45</sup>, with a bulk density of  $1.76 \text{ g cm}^{-3}$ , flexural strength of 203 MPa, compressive strength over 303 MPa, and electrical conductivity of  $3.84 \times 10^4 \text{ S m}^{-1}$ . In contrast to the lengthy and costly CVD-based PyC fabrication<sup>44–46</sup>, the polymer pyrolysis approach offers a simpler, faster, and more economical route to dense carbon materials with comparable performance.

The compressive stress-strain curve of the micro-scale PG-900-s sample is shown in Fig. 4e, with compressive strength reaching 3420 MPa, and the mechanical loading process documented in Video file S1. Notably, the failure of the PG-900-s sample in the micropillar compression test exhibits multiple cracks perpendicular to the compressive stress direction (Supplementary Fig. 16). This behavior differs significantly from the brittle fractures seen in traditional GCM, highlighting the unique microstructure of the GAC. It is worth noting that the compressive strength measured from in-situ SEM micro-pillar tests ( $\sim 3420 \text{ MPa}$ ) significantly exceeds the macroscopic value ( $\sim 303 \text{ MPa}$ ). This difference primarily arises from the intrinsic size effect: micro-scale specimens possess highly uniform structures and minimal defects, revealing the intrinsic strength of the carbon matrix, while bulk samples reflect the flaw-sensitive engineering strength. Furthermore, the nanopillar tests provide direct visualization of crack initiation and propagation, offering mechanistic insight that complements bulk-level observations. Figure 4f presents the nanoscale tensile sample under the TEM view and corresponding stress-strain curve for the PG-900-s, which achieves a tensile strength of 3553 MPa. The loading process is detailed in Supplementary Fig. 17 and Video file S2. The few-layer continuous graphene in PG-900-s is closely linked to its exceptional mechanical properties. During tensile failure, the few-layer graphene acts as a shield, protecting the internal amorphous carbon. When cracks encounter the reinforcing graphene, they are deflected instead of penetrating through, leaving the graphene structures intact post-fracture and consuming more energy. Since flexural tests involve tensile and compressive stresses on opposite sides, the ultra-high tensile and compressive strengths contribute to the GAC record-breaking flexural strength. The tensile and compressive strengths of the micro- and nanoscale samples further confirm that the PG-900-s

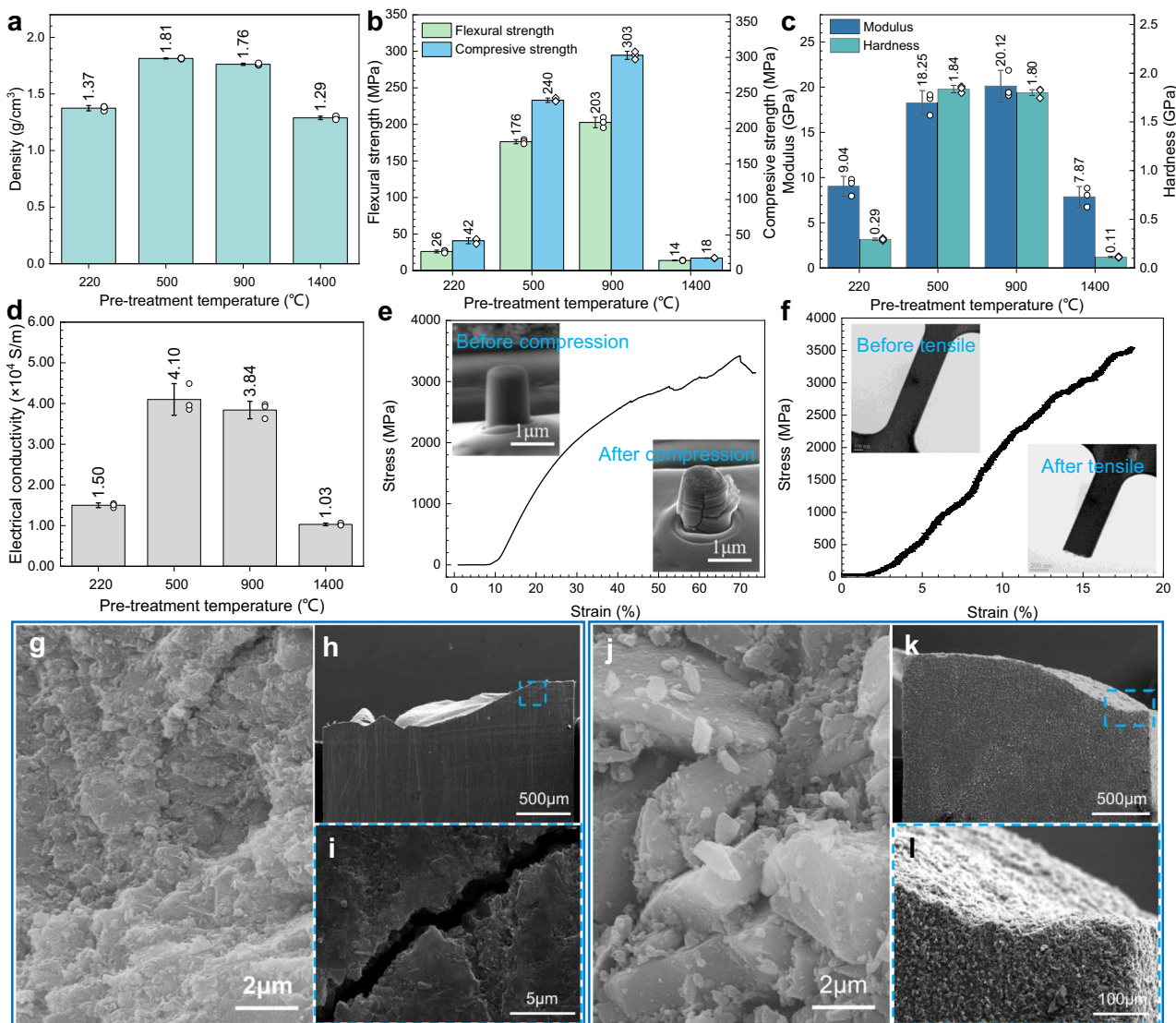


**Fig. 4 | Properties and fracture mechanism of SPS-sintered samples.** **a** Density comparison. **b** Comparison of flexural strength and compressive strength. **c** Comparison of elastic modulus and hardness. **d** Comparison of electrical conductivity. **e** In-situ SEM micro-pillar compression stress-strain curve of the PG-900-s sample, with insets showing the sample's state before and after compression. **f** In-situ TEM tensile stress-strain curve of the PG-900-s sample, with insets showing the sample's state before and after tensile testing. **g–i** Fracture surface morphology,

side view, and enlarged view of the blue box in **h** of PG-900-s. **j–l** Fracture surface morphology, side view and enlarged view of the blue box in **k** of PG-1400-s. The error bars in **a–d** represent individual deviations from three parallel measurements, with data presented as mean values  $\pm$  individual deviations. Each experiment in Figures **g–l** was independently repeated three times with similar results. Source data are provided as a Source Data file.

GAC, with its 3D interconnected structure, exhibits exceptional mechanical properties.

The flexural strength of the PG-900-s sample is significantly higher than that of previously obtained GCM, as illustrated in Fig. 1a. To investigate the strengthening and fracture mechanisms, we analyzed the fractographs and side profiles of the fracture surfaces from flexural samples using scanning electron microscopy (SEM). The fractograph of the PG-900-s sample reveals numerous microscopic dimples (Fig. 4g). The side profile of the fracture surface appears irregular and convoluted, with visible secondary cracks (Fig. 4h, i). The process of flexural and fracture can be inferred from the fracture morphology. Initially, microcracks or voids form in the lower-strength amorphous regions. The crack propagation is hindered by the higher-strength graphene, causing cracks to accumulate and eventually lead to fracture. Due to the continuous graphene networks, a rough fracture surface with microscopic dimples is formed, distinguishing it from the fracture process of traditional graphite. In contrast, the

fractograph of the PG-1400-s sample shows coarse flat planes (Fig. 4j). These planes may result from the fracture at the interface between coarse graphite and amorphous carbon or from the cleavage of graphite grains. The side profile of the PG-1400-s fracture surface is relatively straight with minimal undulation (Fig. 4k, l), suggesting the crack faced few deflections during propagation. Consequently, the PG-1400-s sample exhibits low flexural and compressive strengths.

To further verify the source of the high strength of the PG-900-s, the tensile fracture process was observed in real-time under in-situ HRTEM tensile conditions (Fig. 5 and Video file S3). Initially, microvoids nucleate within the amorphous carbon, causing the crack to expand rapidly before deflecting upon encountering the edges of few-layer graphene sheets<sup>47</sup>. These graphene-induced deflections create a serrated crack appearance as the crack merges with newly formed microvoids. This deflection dissipates energy, thereby enhancing the strength of the GAC<sup>48</sup>. Additionally, the region near the fracture surface experiences amorphization, accompanied by rapid stress

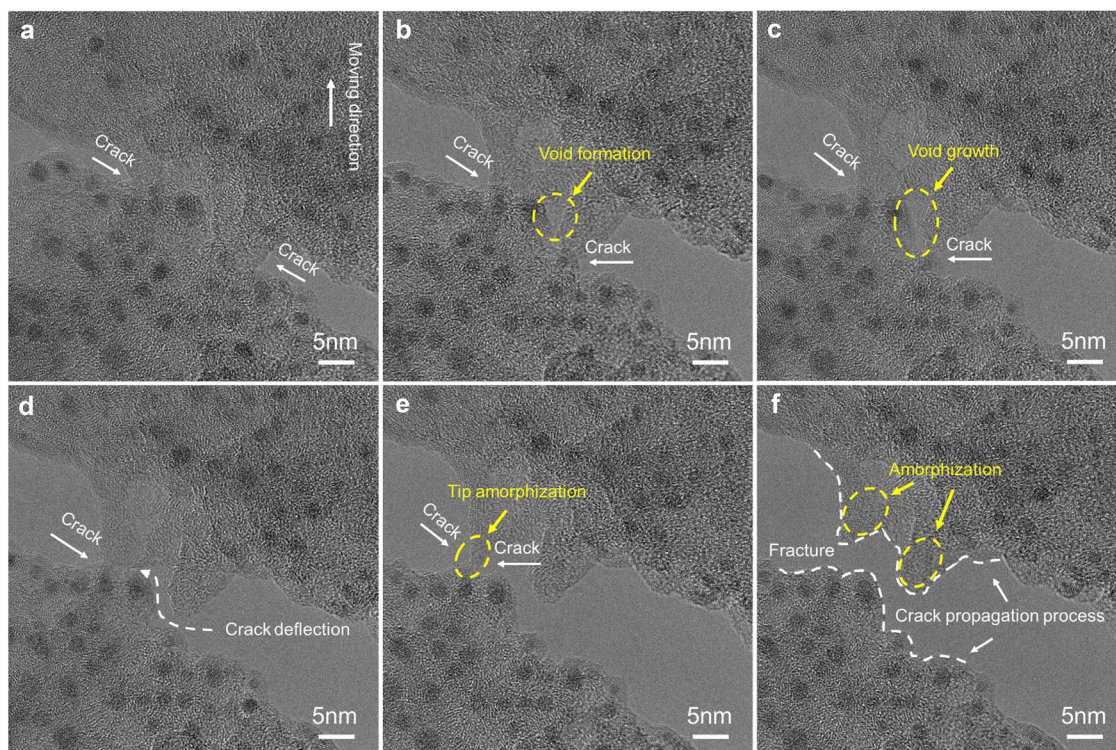


**Fig. 5 | Dynamic crack propagation process under in-situ HRTEM tensile conditions. a** Crack propagation. **b** Void formation. **c** Void growth. **d** Crack deflection. **e** Tip amorphization. **f** Fracture. Each experiment in **a–f** was independently repeated three times with similar results.

relaxation and strain recovery<sup>49</sup>. Ultimately, after undergoing void formation and growth, crack deflection, and amorphous transformation, the sample fractures.

In conclusion, PAM and GLC were selected as starting materials to prepare bulk graphene-amorphous carbon (GAC) using a two-step strategy involving pre-treatment and the SPS method. By strategically leveraging the structural characteristics of PAM and GLC during gelation and polymerization, as well as their structural inheritance during pyrolysis, we engineered a distinctive interwoven graphene network that imparts exceptional properties. The GAC developed in this study surpasses the performance limitations of traditional GCM, underscores the importance of microstructural design and control in optimizing the properties of graphite-based carbon materials, and provides a pathway for developing high-strength materials.

## Methods

### Sample synthesis

Glucose monohydrate ( $\geq 98\%$  purity, analytical/pharmaceutical grade, product No.: G107849, Shanghai Aladdin Bio-Chem Technology Co., Ltd.) derived from cornstarch via a double-enzyme hydrolysis process, followed by decolorization, ion exchange, and crystallization, was used without further purification. Its specific optical rotation ( $+52.6$  to  $+53.2^\circ$ ) confirmed an equilibrium ratio ( $-36\%:64\%$ ) of  $\alpha$ - and  $\beta$ -pyranose isomers, with isomer purity exceeding 98%. Acrylamide (purity  $\geq 99\%$ , product No.: A103591, Aladdin) with a melting point range of  $83$ – $87^\circ\text{C}$  and a monomer molecular weight of  $71.08\text{ g/mol}$ , as well as  $N,N'$ -methylenebisacrylamide (MBA, purity  $\geq 99\%$ , electrophoresis grade, product No.: M102752, Aladdin), synthesized by acrylamide-formaldehyde condensation, were employed directly as received. Detailed batch certificates of analysis (COA) for all materials, including moisture content, inorganic impurities, and structural confirmation by  $^1\text{H}$  NMR and FTIR spectroscopy, assured material consistency and reproducibility.

For the hydrogel precursor preparation, glucose monohydrate (200 g), acrylamide (60 g), and MBA (1.5 g) were dissolved in 550 g of deionized water under mechanical stirring at room temperature ( $-25^\circ\text{C}$ ), with humidity maintained between 50% and 70%, for 60 minutes to achieve homogeneous dispersion. The obtained clear solution was subsequently placed in an oven at  $60^\circ\text{C}$  to undergo gelation and drying for 24 hours. The dried hydrogel was pre-carbonized in a muffle furnace at a heating rate of  $0.5^\circ\text{C/min}$  to  $220^\circ\text{C}$  and held for 2 hours, yielding the PG-220 intermediate. Further carbonization was performed in a tube furnace under vacuum at heating rates of  $4^\circ\text{C/min}$  to  $500^\circ\text{C}$ ,  $900^\circ\text{C}$ , and  $1400^\circ\text{C}$ , each temperature maintained for 1 hour, producing samples PG-500, PG-900, and PG-1400, respectively. The pre-treatment temperatures ( $220^\circ\text{C}$ ,  $500^\circ\text{C}$ ,  $900^\circ\text{C}$ , and  $1400^\circ\text{C}$ ) were carefully selected based on detailed TG/DTG analysis. These temperatures correspond respectively to the completion of caramelization and Maillard reactions ( $220^\circ\text{C}$ ), PAM decomposition ( $500^\circ\text{C}$ ), optimized nitrogen-mediated partial graphitization ( $900^\circ\text{C}$ ), and near-complete nitrogen removal and final structural stabilization through high-temperature carbonization ( $1400^\circ\text{C}$ )<sup>26,29</sup>.

The carbonized samples were initially ground into sub-millimeter powders using an agate mortar and subsequently ball-milled at 200 rpm for 6 hours to yield micron-sized powders. Finally, dense bulk composites were fabricated via spark plasma sintering (SPS) at  $2400^\circ\text{C}$  under 60 MPa pressure, with a heating rate of  $150^\circ\text{C/min}$  and a holding time of 10 minutes. The density of the sintered specimens was measured using Archimedes' principle.

### Scanning electron microscopy (SEM)

The surface, cross-sectional, and fracture morphologies of the powder and bulk samples were observed and recorded using a scanning electron microscope (SEM, TESCAN CLARA, Zeiss Merlin Compact) at an accelerating voltage of 20 kV.

### Cryo-scanning electron microscopy (Cryo-SEM)

The morphology of the PG hydrogel samples was examined using a cryo-scanning electron microscope (Cryo-SEM, Regulus8220). Prior to observation, conductive carbon adhesive was applied to the sample stage, and samples were mounted using tweezers. The sample stage with the mounted samples was then rapidly frozen in liquid nitrogen slush for 30 seconds. A low-temperature preparation transfer system was used to transfer the samples under vacuum to the preparation chamber for sublimation and gold coating. The samples were sublimated at -90 °C for 10 minutes, followed by gold sputtering at 10 mA for 60 seconds. Finally, the samples were observed in the SEM chamber at a cold stage temperature of -140 °C and an accelerating voltage of 5 kV.

### Transmission electron microscopy (TEM)

The microstructure of the samples was analyzed using transmission electron microscopy (TEM). For powder samples, the material was dispersed in anhydrous ethanol, ultrasonicated, and then dropped onto a holey carbon grid. After drying, observations were conducted at an accelerating voltage of 200 kV using an FEI Talos F200X TEM. For the bulk carbon materials obtained via SPS sintering, focused ion beam (FIB) milling (TESCAN CLARA) was used to extract and thin micro-scale samples to approximately 50 nm, which were then transferred to TEM grids. During FIB processing, the voltage and current were gradually reduced from 20 kV and 0.6-1 nA to 5 kV and 20-30 pA. Final polishing was performed at 5 kV and 10 pA. Microstructural observations were carried out using FEI Talos F200X and FEI Tecnai G2 F20 TEMs.

### X-ray diffraction analysis (XRD)

The phase composition of the samples was analyzed using an X-ray diffractometer (Empyrean, Panalytical) with a copper target ( $K\alpha$ ,  $\lambda = 1.5406 \text{ \AA}$ ). A step size of  $0.05^\circ$  and a time interval of 0.5 s were used.

### Raman spectroscopy analysis

Defect and stacking configurations of the samples were analyzed using a tip-enhanced laser confocal Raman spectroscopy system (inVia-Reflex, Renishaw) with a laser wavelength of 532 nm.

### X-ray Photoelectron Spectroscopy (XPS) valence state analysis

Chemical bonding and semi-quantitative elemental analysis were performed using an X-ray photoelectron spectrometer (Thermo Fisher Scientific) with an Al  $K\alpha$  X-ray source (1486 eV). The measurement step size was 0.1 eV.

### Fourier transform infrared spectroscopy (FTIR)

Functional groups in the samples were analyzed using a Fourier transform infrared spectrometer (Nicolet iS50). The spectra were recorded in the range of  $4000$  to  $400 \text{ cm}^{-1}$  with a wavenumber accuracy of  $0.005 \text{ cm}^{-1}$ .

### Mercury intrusion porosimetry (MIP)

A mercury intrusion porosimeter (MIP, Micromeritics AutoPore V 9620) was employed to characterize the pore size distribution and porosity of bulk carbon materials.

### Electrical conductivity measurement

The electrical conductivity of bulk materials was measured at room temperature using a resistivity meter (Model 2512, Changsheng Electronic Technology, Suzhou). Test samples, with dimensions of  $2 \times 2 \times 15 \text{ mm}$ , were polished to ensure a smooth, scratch-free surface before testing.

### Flexural and compression testing<sup>15</sup>

The mechanical properties of the samples were evaluated using a universal testing machine (Shimadzu, AGX plus 5KN). The three-point

flexural test samples had dimensions of  $2 \times 2 \times 15 \text{ mm}$  with a loading rate of  $0.5 \text{ mm/min}$ . The compression test samples had dimensions of  $\phi 3 \times 4.5 \text{ mm}$ , with a compression rate of  $0.5 \text{ mm/min}$ . The mechanical tests were performed on three independent specimens for both flexural and compressive strength, with the average values reported.

The Flexural strength ( $\sigma_f$ ) was calculated using the following parameters:

$$\sigma_f = \frac{3P_f L}{2bh^2} \quad (1)$$

$\sigma_f$  – Flexural strength (MPa);

$P_f$  – maximum load (N);

$L$  – span length (mm);

$h$  – sample height (mm);

$b$  – sample width (mm).

The formula for calculating compressive strength ( $\sigma_c$ ) is:

$$\sigma_c = \frac{P}{A} \quad (2)$$

$\sigma_c$  – compressive strength (MPa);

$P$  – applied load (N);

$A$  – load-bearing area ( $\text{mm}^2$ ).

### Nanoindentation testing<sup>5</sup>

Sample hardness and modulus were measured using a nanoindenter (G200, Keysight), which provided load-displacement curves. All samples were finely polished to a mirror finish before testing. During nanoindentation, a linear load was applied over 15 seconds up to a maximum load of 10 mN, held for 10 seconds, and then released over 15 seconds.

### In-situ compression testing in scanning electron microscope<sup>18,50,51</sup>

In-situ compression testing of the micro-scale PG-900-s samples was conducted using a Hysitron PI-88 mechanical tester integrated within a scanning electron microscope (SEM, Helios 600, FEI). Prior to testing, micropillars were fabricated with a diameter of approximately  $1 \mu\text{m}$  and a height of about  $1.5 \mu\text{m}$ , as illustrated in Supplementary Fig. 1. During testing, a B-type diamond nanoindenter with a diameter of  $5 \mu\text{m}$  was used to compress the top of the micropillars at a constant displacement rate of  $1 \text{ nm/s}$ . A high-load sensor integrated with the testing apparatus captured the deformation characteristics of the micropillars in real time. The direct compression loading process is documented in Video S1.

### In-situ tensile testing in transmission electron microscope (TEM)<sup>41,52,53</sup>

PG-900-s T-shaped bridge tensile samples were prepared using focused ion beam (FIB) milling (Helios Nanolab 600i). Initial sculpting and final thinning were performed using gallium ion beam currents ranging from  $15 \text{ nA}$  at  $20 \text{ kV}$  to  $10 \text{ pA}$  at  $5 \text{ kV}$ , as detailed in Supplementary Fig. 2. Based on top-view and side-view SEM and TEM images, the effective dimensions of the T-shaped bridge tensile samples were determined to be approximately  $300 \text{ nm}$  in width,  $160 \text{ nm}$  in thickness, and  $1.5 \mu\text{m}$  in length. In-situ tensile and cyclic loading tests were conducted using a Hysitron PI 95 TEM PicoIndenter in a transmission electron microscope (JEOL JEM-2100F,  $200 \text{ kV}$ ) at a tensile rate of  $1 \text{ nm/s}$ , with the entire process observed and recorded via TEM. The loading process is shown in Video S2.

## In-situ high-resolution transmission electron microscopy (HRTEM) tensile testing<sup>54–57</sup>

HRTEM observations were performed on an FEI Talos F200X transmission electron microscope at 200 kV. Time-resolved HRTEM images were recorded at a rate of five frames per second. Samples were mounted on a TEM holder using equipment developed by Bestron (Beijing) Science and Technology Co., LTD., enabling in-situ deformation. The samples were controlled via an integrated microelectromechanical system (MEMS) chip, with the deformation unit driven by a lead zirconate titanate (PZT) actuator under displacement control. The PZT actuator provided a full travel range of 4  $\mu\text{m}$ , with a step size of 0.1 nm, a maximum load of 1 N, and a resolution of 1 nN. The tensile rate was set to 0.5 nm/s. The loading process is documented in Video S3. Micronano tensile samples were prepared using FIB prior to testing, as detailed in Supplementary Fig. 3.

### Reporting summary

Further information on research design is available in the Nature Portfolio Reporting Summary linked to this article.

### Data availability

The data that support the findings of this study are available within this article and its Supplementary Information. Further data are available from the corresponding authors upon request. Source data are provided with this paper.

### References

1. Ma, T. et al. Tailoring the thermal and electrical transport properties of graphene films by grain size engineering. *Nat. Commun.* **8**, 14486 (2017).
2. Li, P. et al. Bidirectionally promoting assembly order for ultrastiff and highly thermally conductive graphene fibres. *Nat. Commun.* **15**, 409 (2024).
3. Shang, Y. et al. Ultrahard bulk amorphous carbon from collapsed fullerene. *Nature* **599**, 599–604 (2021).
4. Bai, X. Nitrogen-doped amorphous monolayer carbon. *Nature* **634**, 80–84 (2024).
5. Lin, K. et al. Ultra-strong nanographite bulks based on a unique carbon nanotube linked graphite onions structure. *Carbon* **149**, 436–444 (2019).
6. Zhang, Y. et al. Heat dissipation of carbon shell in ZrC–SiC/TaC coating to improve protective ability against ultrahigh temperature ablation. *J. Adv. Ceram.* **13**, 1080–1091 (2024).
7. Cabiellles, M., Montes-Morán, M. A. & Garcia, A. B. Structural study of graphite materials prepared by HTT of unburned carbon concentrates from coal combustion fly ashes. *Energy Fuels* **22**, 1239–1243 (2008).
8. Nomura, S. & Arima, T. Influence of binder (coal tar and pitch) addition on coal caking property and coke strength. *Fuel Process. Technol.* **159**, 369–375 (2017).
9. Qiu, H., Song, Y., Liu, L., Zhai, G. & Shi, J. Thermal conductivity and microstructure of Ti-doped graphite. *Carbon* **41**, 973–978 (2003).
10. Liu, Z., Guo, Q., Shi, J., Zhai, G. & Liu, L. Graphite blocks with high thermal conductivity derived from natural graphite flake. *Carbon* **46**, 414–421 (2008).
11. Tan, J. et al. Enhanced self-sintering mechanical strength of carbon blocks via removal of light molecular-weight compound in green petroleum coke. *Fuel* **343**, 127912 (2023).
12. Li, J. et al. Bridging graphene sheets to ultra-high-performance graphene-based bulk materials via Si-C bonding and Y-type carbon structure. *Carbon* **217**, 118619 (2024).
13. Liu, Z., Guo, Q., Shi, J., Zhai, G. & Liu, L. Preparation of doped graphite with high thermal conductivity by a liquid mixing process. *Carbon* **45**, 1914–1916 (2007).
14. Tu, C. et al. Superior mechanical properties of sulfonated graphene reinforced carbon-graphite composites. *Carbon* **148**, 378–386 (2019).
15. Lin, K. et al. Nanoburl Graphites. *Adv. Mater.* **33**, 2007513 (2021).
16. Li, J. et al. Improving the performance of carbon/graphite composites through the synergistic effect of electrostatic self-assembled carbon nanotubes and nano carbon black. *Ceram. Int.* **48**, 36029–36037 (2022).
17. Li, Z. et al. Ultrastrong conductive in situ composite composed of nanodiamond incoherently embedded in disordered multilayer graphene. *Nat. Mater.* **22**, 42–49 (2023).
18. Sun, B. et al. Sugar-Derived Isotropic Nanoscale Polycrystalline Graphite Capable of Considerable Plastic Deformation. *Adv. Mater.* **34**, 2200363 (2022).
19. Feng Y. Development of homogeneous graphites by cold isostatic pressure in Japan. *Carbon Tech.* 21–26 (2001) <https://doi.org/10.3969/j.issn.1001-3741.2001.02.006>.
20. Feng, J. ie & Feng, Y. ongyang Development of homogeneous graphite by cold isostatic pressure in America, Germany, France, Russia and Poland. *Carbon Tech.* **24**, 32–36 (2005).
21. Xia, L. ibo et al. Current status for preparation and research of graphite materials with high density and high strength. *Carbon Tech.* **27**, 24–27 (2008).
22. Li, B. et al. Discovery of Gradia between Graphite and Diamond. *Acc. Mater. Res.* **5**, 614–624 (2024).
23. Wang, L. et al. Long-range ordered carbon clusters: a crystalline material with amorphous building blocks. *Science* **337**, 825–828 (2012).
24. Luo, K. et al. Coherent interfaces govern direct transformation from graphite to diamond. *Nature* **607**, 486–491 (2022).
25. Zhang, L. et al. Microstructure graphitization evolution and multi-scale, multi-mechanism synergistic enhancement of ultra-high strength carbon-graphite materials. *Diam. Relat. Mater.* **128**, 109271 (2022).
26. Yang, Y. et al. Eco-friendly and sustainable approach of assembling sugars into biobased carbon fibers. *Green. Chem.* **24**, 5097–5106 (2022).
27. Yang, Y. et al. Nature-inspired self-activation method for the controllable synthesis of highly porous carbons for high-performance supercapacitors. *Carbon* **205**, 1–9 (2023).
28. Zhang, W. et al. Sugar-derived nanocrystalline graphite Matrix C/C composites with excellent ablative resistance at 3000. *C. Adv. Mater.* **36**, 2309899 (2024).
29. Tan, M. et al. Anisotropically oriented carbon films with dual-function of efficient heat dissipation and excellent electromagnetic interference shielding performances. *Adv. Funct. Mater.* **32**, 2202057 (2022).
30. Deokar, G., Jin, J., Schwingenschlöggl, U. & Costa, P. M. F. J. Chemical vapor deposition-grown nitrogen-doped graphene's synthesis, characterization and applications. *Npj 2D Mater. Appl.* **6**, 14 (2022).
31. Morishita, T. et al. Carbon fibre production using an ecofriendly water-soluble precursor. *Nat. Commun.* **16**, 4614 (2025).
32. Zhang, Q. et al. Defects boost graphitization for highly conductive graphene films. *Natl. Sci. Rev.* **10**, nwad147 (2023).
33. Hemmler, D. et al. Evolution of complex Maillard chemical reactions, resolved in time. *Sci. Rep.* **7**, 3227 (2017).
34. Titirici, M.-M., Thomas, A. & Antonietti, M. Replication and coating of silica templates by hydrothermal carbonization. *Adv. Funct. Mater.* **17**, 1010–1018 (2007).
35. Toh, C.-T. et al. Synthesis and properties of free-standing monolayer amorphous carbon. *Nature* **577**, 199–203 (2020).
36. Kravchenko, O. G. et al. Modeling compressive behavior of open-cell polymerized high internal phase emulsions: effects of density and morphology. *Soft Matter* **14**, 1637–1646 (2018).

37. Barg, S. et al. Mesoscale assembly of chemically modified graphene into complex cellular networks. *Nat. Commun.* **5**, 4328 (2014).
38. Wang, X. et al. Three-dimensional strutted graphene grown by substrate-free sugar blowing for high-power-density supercapacitors. *Nat. Commun.* **4**, 2905 (2013).
39. Sadezky, A., Muckenhuber, H., Grothe, H., Niessner, R. & Pöschl, U. Raman microspectroscopy of soot and related carbonaceous materials: Spectral analysis and structural information. *Carbon* **43**, 1731–1742 (2005).
40. Cançado, L. G. et al. General equation for the determination of the crystallite size  $L_a$  of nanographite by Raman spectroscopy. *Appl. Phys. Lett.* **88**, 163106 (2006).
41. Zhang, X. et al. Theoretical strength and rubber-like behaviour in micro-sized pyrolytic carbon. *Nat. Nanotechnol.* **14**, 762–769 (2019).
42. Leyssale, J.-M., Couégnat, G., Jouannigot, S. & Vignoles, G. L. Mechanisms of elastic softening in highly anisotropic carbons under in-plane compression/indentation. *Carbon* **197**, 425–434 (2022).
43. López-Honorato, E., Meadows, P. J. & Xiao, P. Fluidized bed chemical vapor deposition of pyrolytic carbon – I. Effect of deposition conditions on microstructure. *Carbon* **47**, 396–410 (2009).
44. Zhang, D. et al. Coefficients of thermal expansion of low texture and isotropic pyrocarbon deposited on stationary substrates. *Mater. Lett.* **68**, 68–70 (2012).
45. Ren, J., Li, K., Zhang, S., Yao, X. & Li, H. Preparation of high texture three-dimensional braided carbon/carbon composites by pyrolysis of ethanol and methane. *Ceram. Int.* **42**, 2887–2891 (2016).
46. Tan, R. et al. A new approach to fabricate superhydrophobic and antibacterial low density isotropic pyrocarbon by using catalyst free chemical vapor deposition. *Carbon* **145**, 359–366 (2019).
47. Wu, Y. et al. Twisted-layer boron nitride ceramic with high deformability and strength. *Nature* **626**, 779–784 (2024).
48. Yue, Y. et al. Hierarchically structured diamond composite with exceptional toughness. *Nature* **582**, 370–374 (2020).
49. Li, Z. et al. Nanoporous amorphous carbon nanopillars with lightweight, ultrahigh strength, large fracture strain, and high damping capability. *Nat. Commun.* **15**, 8151 (2024).
50. Tang, D.-M. et al. Size Effects on the Mechanical Properties of Nanoporous Graphene Networks. *Adv. Funct. Mater.* **29**, 1900311 (2019).
51. Greer, J. R., Oliver, W. C. & Nix, W. D. Size dependence of mechanical properties of gold at the micron scale in the absence of strain gradients. *Acta Mater.* **53**, 1821–1830 (2005).
52. Dong, L. R. et al. Borrowed dislocations for ductility in ceramics. *Science* **385**, 422–427 (2024).
53. Dang, C. et al. Achieving large uniform tensile elasticity in micro-fabricated diamond. *Science* **371**, 76–78 (2021).
54. Qiu, K. et al. Self-healing of fractured diamond. *Nat. Mater.* **22**, 1317–1323 (2023).
55. Wang, L. et al. Tracking the sliding of grain boundaries at the atomic scale. *Science* **375**, 1261–1265 (2022).
56. Wang, L. et al. In situ atomic-scale observation of grain size and twin thickness effect limit in twin-structural nanocrystalline platinum. *Nat. Commun.* **11**, 1167 (2020).
57. Zhang, J. et al. Timely and atomic-resolved high-temperature mechanical investigation of ductile fracture and atomistic mechanisms of tungsten. *Nat. Commun.* **12**, 2218 (2021).

## Acknowledgements

This work is supported by the Key Program of National Natural Science Foundation of China (No. 52032003).

## Author contributions

X. Z., W. F., L. W. and J. S. conceived the project. W. C., J. S., W. F., D. C., and X. Z. designed the experiments. W. C., B. L., D. Z., L. Z. and X. L. synthesized the samples. Y. W., Y. L. and Y. F. conducted the XRD measurements. W. C., L. Z. and X. L. performed the infrared and Raman spectroscopy tests. W. C., Q. R. and D. Z. carried out the three-point flexural, compression and nanoindentation tests. W. C. and B. L. performed the electrical conductivity and density measurements. W. C., B. S., W. Z. and M. T. conducted SEM, Cryo-SEM, and in-situ SEM compression tests. Q. L. performed the XPS analysis. W. C. and H. D. conducted the TEM tests, while W. C., P. Z. and P. C. Z. prepared T-shaped bridge samples and performed the in-situ TEM tensile tests. W. C., H. D., Y. Z., X. Y. and Z. W. conducted the in-situ high-resolution TEM sample preparation and testing. W. C., J. S., W. F., Y. C., S. D., S. Y. D., J. H. and W. L. analyzed the data. W. C., J. S. and W. F. co-wrote the manuscript. All authors discussed the results and commented on the manuscript.

## Competing interests

The authors declare no competing interests.

## Additional information

**Supplementary information** The online version contains supplementary material available at <https://doi.org/10.1038/s41467-025-65877-8>.

**Correspondence** and requests for materials should be addressed to Jie Sheng, Lidong Wang, Weidong Fei or Xinghong Zhang.

**Peer review information** *Nature Communications* thanks Oleksandr G. Kravchenko, and the other, anonymous, reviewer(s) for their contribution to the peer review of this work. A peer review file is available.

**Reprints and permissions information** is available at <http://www.nature.com/reprints>

**Publisher's note** Springer Nature remains neutral with regard to jurisdictional claims in published maps and institutional affiliations.

**Open Access** This article is licensed under a Creative Commons Attribution-NonCommercial-NoDerivatives 4.0 International License, which permits any non-commercial use, sharing, distribution and reproduction in any medium or format, as long as you give appropriate credit to the original author(s) and the source, provide a link to the Creative Commons licence, and indicate if you modified the licensed material. You do not have permission under this licence to share adapted material derived from this article or parts of it. The images or other third party material in this article are included in the article's Creative Commons licence, unless indicated otherwise in a credit line to the material. If material is not included in the article's Creative Commons licence and your intended use is not permitted by statutory regulation or exceeds the permitted use, you will need to obtain permission directly from the copyright holder. To view a copy of this licence, visit <http://creativecommons.org/licenses/by-nc-nd/4.0/>.

© The Author(s) 2025